Check for updates

Intrinsic lifetime of higher excitonic states in tungsten diselenide monolayers†

Samuel Brem, [ID] *[a] Jonas Zipfel,[b] Malte Selig, [ID] [c] Archana Raja, [ID] [d]
Lutz Waldecker, [ID] [e] Jonas D. Ziegler,[b] Takashi Taniguchi,[f] Kenji Watanabe, [ID] [f]
Alexey Chernikov[b] and Ermin Malic[a]

The reduced dielectric screening in atomically thin transition metal dichalcogenides allows to study the hydrogen-like series of higher exciton states in optical spectra even at room temperature. The width of excitonic peaks provides information about the radiative decay and phonon-assisted scattering channels limiting the lifetime of these quasi-particles. While linewidth studies so far have been limited to the exciton ground state, encapsulation with hBN has recently enabled quantitative measurements of the broadening of excited exciton resonances. Here, we present a joint experiment–theory study combining microscopic calculations with spectroscopic measurements on the intrinsic linewidth and lifetime of higher exciton states in hBN-encapsulated WSe_2 monolayers. Surprisingly, despite the increased number of scattering channels, we find both in theory and experiment that the linewidth of higher excitonic states is similar or even smaller compared to the ground state. Our microscopic calculations ascribe this behavior to a reduced exciton–phonon scattering efficiency for higher excitons due to spatially extended orbital functions.

Monolayer transition metal dichalcogenides (TMDs) show pronounced Coulomb phenomena,[1–7,40] which in bulk materials become observable predominantly at very low temperatures. Electron–hole pairs in TMDs exhibit binding energies of up to 0.5 eV giving rise to a Rydberg-like series of exciton states below the free particle bandgap.[8–12] While the relative position of excitonic resonances in optical spectra presents a fingerprint of Coulomb correlations,[13–15] their linewidth contains information about their coherence lifetime and the underlying many-particle scattering processes. Previous studies on exciton linewidths in TMDs[16–19] have revealed efficient scattering into dark intervalley excitons[20] and have demonstrated strain-induced modifications of exciton–phonon scattering channels.[21,41] However, these studies have been restricted to the 1s exciton ground state, since the higher order resonances were dominated by inhomogeneous broadening and were challenging to resolve and analyze at elevated temperatures.

Furthermore, exciton–phonon scattering within the rich phase space of excited exciton states has not been theoretically investigated in TMDs yet. Recently, the encapsulation of TMD materials in the layered wide-bandgap insulator hexagonal boron nitride (hBN) has been shown to drastically reduce the inhomogeneous broadening of excitonic resonances[11,12] and thereby enables access to temperature-dependent broadening of higher excitonic states.

In this work, we present a joint experiment-theory study on the homogeneous broadening of higher excitonic resonances and the underlying microscopic scattering mechanism for the exemplary case of hBN-encapsulated monolayer tungsten diselenide (WSe_2). Our calculations based on the density matrix formalism provide microscopic access to radiative decay and phonon-assisted exciton scattering channels across the full Rydberg-like series of excitonic states including intervalley excitons and symmetry forbidden dark states (*e.g.* p-type excitons), *cf.* Fig. 1. The microscopic model is supported by reflectance contrast measurements on hBN-encapsulated WSe_2 monolayers, providing temperature-dependent linewidths of the three energetically lowest exciton resonances 1s, 2s and 3s. We reveal that although excited states exhibit a much larger phase space for possible relaxation channels, their linewidth stays comparable with the ground state and even decreases for states above 2s excitons. This reflects the increase of the exciton Bohr radii for excited states, which results in reduced excitonic form factors due to a smaller overlap of the initial

[a]Chalmers University of Technology, Department of Physics, 41296 Gothenburg, Sweden. E-mail: samuel.brem@chalmers.se
[b]University of Regensburg, Department of Physics, 93053 Regensburg, Germany
*[c]Technical University Berlin, Institute of Theoretical Physics, 10623 Berlin, Germany*
[d]Kavli Energy NanoScience Institute, University of California Berkeley, Berkeley, USA
[e]Stanford University, 348 Via Pueblo Mall, Stanford, California 94305, USA
[f]National Institute for Materials Science, Tsukuba, Ibaraki 305-004, Japan
†Electronic supplementary information (ESI) available. See DOI: 10.1039/C9NR04211C
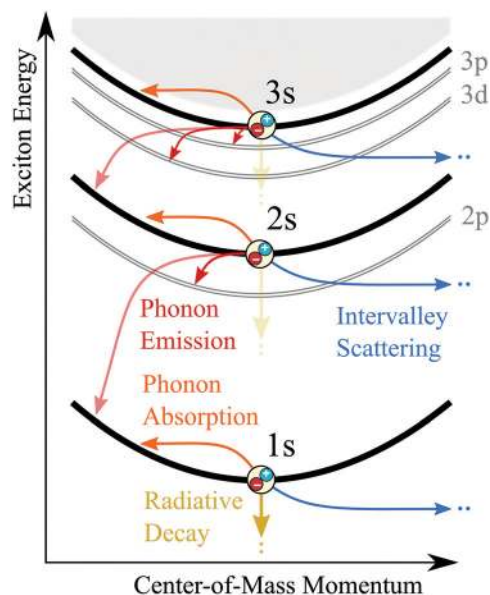
Fig. 1 Schematic illustration of the exciton bandstructure and possible scattering mechanisms. Optically generated excitons at zero center-of-mass momentum can decay either by radiative recombination (yellow arrow) or by scattering into a dark state with finite center-of-mass momentum. Apart from intravalley scattering *via* absorption of acoustic phonons (orange) or transitions into lower lying states after emission of a phonon (red), electron or hole can scatter into a different valley creating an intervalley exciton (blue).

and final state wavefunctions in momentum space and thus a quenched exciton–phonon scattering efficiency.

Theoretical approach

To calculate the optical response of TMD monolayers, we use the Heisenberg equation of motion to derive the semiconductor Bloch equations.[22–24] Here, we explicitly include the exciton–phonon interaction to account for non-radiative broadening of excitonic resonances. Moreover, we consider the Coulomb interaction on a Hartree–Fock level, which yields an excitonic renormalization of interband transitions as well as exciton–phonon transition energies. Within a second order Born–Markov approximation the linear optical absorption of a circularly (σ)-polarized field reads[23]

$$\alpha_\sigma(\omega) = \frac{e_0{}^2}{m_0{}^2\varepsilon_0 n c_0 \omega} |M_\sigma|^2 \sum_\nu \Im m\left(\frac{|\Phi_\nu(r=0)|^2}{E_\nu - \hbar\omega - i\Gamma_\nu}\right). \quad (1)$$

Here, we used the *p·A* gauge, so that the overall strength of the response is determined by the projection of the interband momentum matrix element on the light polarization M_σ, which is determined analytically within a two band *k·p* approach,[25] *cf.* ESI†. The constants e_0 and m_0 denote the elementary charge and the electron rest mass, while c_0 and n are the vacuum light velocity and refractive index, respectively. Furthermore, the optical response is given by a sum of

Lorentzian peaks, whose position and oscillator strength is determined by the eigen energy E_ν and wavefunctions Φ_ν of exciton states ν. The latter are obtained by solving the Wannier equation[22,23,26] within an effective mass approximation and a thin-film approximation of the Coulomb potential to account for a non-uniform dielectric environment.[27,28] Details about the solution of the Wannier equation and the used *ab initio* parameters[29,30] are given in the ESI.†

The decay rate $\Gamma_\nu = \Gamma_\nu^{\mathrm{phon}} + \Gamma_\nu^{\mathrm{rad}}$ determines the broadening of excitonic resonances in an absorption spectrum. It corresponds to the inverse lifetime of coherent excitons, *i.e.* optically generated excitons at zero center-of-mass momentum. They can decay either by recombination $\Gamma_\nu^{\mathrm{rad}}$ (radiative dephasing) or scattering with phonons $\Gamma_\nu^{\mathrm{phon}}$ into a state with finite center-of-mass momentum. Taking into account a self-consistent coupling between the light field and the induced microscopic polarization,[23,31] we obtain the radiative broadening

$$\Gamma_\nu^{\mathrm{rad}} = \frac{\hbar e_0{}^2}{2m_0{}^2\varepsilon_0 n c_0} |M_\sigma|^2 \frac{|\Phi_\nu(r=0)|^2}{E_\nu}, \quad (2)$$

The non-radiative dephasing due to exciton–phonon-scattering reads[26,32,33]

$$\Gamma_\nu^{\mathrm{phon}} = \pi \sum_{\pm,\lambda,\mu,\mathbf{q}} \left|G_{\lambda\mathbf{q}}^{\nu\mu}\right|^2 \hat{n}_{\lambda\mathbf{q}}^\pm \delta\left(E_\mathbf{q}^\mu - E_0^\nu \pm \hbar\omega_{\lambda\mathbf{q}}\right). \quad (3)$$

Here, the occupation factor $\hat{n}_{\lambda\mathbf{q}}^\pm = \frac{1}{2} \pm \frac{1}{2} + n_{\lambda\mathbf{q}}$ accounts for the number of phonons $n_{\lambda\mathbf{q}}$ in the mode λ and the momentum $\mathbf{q}$ weighting the emission (+) and absorption processes (−). In the applied Markov approximation we require strict energy and momentum conservation for the scattering from the lowest energy state in the light cone $E_{\mathbf{q}=0}^\nu$ to an exciton $E_\mathbf{q}^\mu$ with a non-zero center-of-mass momentum $\mathbf{q}$ under interaction with a phonon with the energy $\hbar\omega_{\lambda\mathbf{q}}$. The scattering cross-section for exciton transitions $(\nu,0) \to (\mu,\mathbf{q})$ is determined by the overlap of the initial and final state exciton wavefunctions in Fourier space $\tilde{\Phi}$ shifted by the scattering momentum and reads

$$G_{\lambda\mathbf{q}}^{\nu\mu} = \sum_{\mathbf{k},\alpha=e,h} g_{\lambda\mathbf{q}}^{\alpha\mathbf{k}} \tilde{\Phi}_\nu^*(\mathbf{k}) \tilde{\Phi}_\mu(\mathbf{k}+\mathbf{q}_\alpha). \quad (4)$$

The relative momentum transferred to the electron (hole) constituent when the entire exciton gains a center-of-mass momentum $\mathbf{q}$ is denoted by $\mathbf{q_{e(h)}}$ with $\mathbf{q} = \mathbf{q_e} + \mathbf{q_h}$. The exciton index ν here acts as a compound index containing principal quantum number, angular momentum, electron/hole valley and spin configuration. For the carrier-phonon coupling g we use the deformation potential approximations for acoustic and optical phonons deduced from density functional perturbation theory (DFPT) in ref. 34. Here, the electron–phonon coupling in the vicinity of high-symmetry points only depends on the transferred momentum $\mathbf{q}$, so that $G_{\lambda\mathbf{q}}^{\nu\mu} \propto \mathcal{F}_{\mu\nu}(\mathbf{q}_\alpha) = \int d^2r\, \Phi_\nu^*(\mathbf{r}) e^{i\mathbf{q}_\alpha\mathbf{r}} \Phi_\mu(\mathbf{r})$. The excitonic form factor $\mathcal{F}_{\nu\mu}$ accounts for the geometry of the exciton wavefunctions involved in the scattering process, which will be crucial for the interpretation of our results.

Throughout this work, we only consider the A-exciton series and thus focus on the spin configuration composing the lowest optically allowed transition at the K point. However we take into account phonon scattering into all minima (maxima) of the conduction (valence) band with the same spin configuration including intervalley scattering of electrons to the Λ, Λ' and K' valley and hole scattering to the Γ or K' point. Furthermore, we include the full excitonic Rydberg series for intra- as well as intervalley excitons reachable *via* phonon-assisted transitions, *cf.* Fig. 1. Further details about the used matrix-elements and the calculation of scattering amplitudes are given in the ESI.†

Exciton spectroscopy

Linear reflectance measurements are performed on a WS_2 monolayer sample encapsulated between ultra-thin layers of hexagonal boron nitride and placed on a SiO_2/Si substrate. The spectra are acquired at lattice temperatures from 5 to 300 K using a spectrally broad whitelight source for illumination. Spectrally-resolved reflectance signals are recorded both on the sample and on the SiO_2/Si substrate reference. The data are presented in terms of reflectance contrast, defined by the relative change in reflectance on the sample with respect to the reference. For quantitative analysis, the optical response is parameterized by a multi-Lorentzian dielectric function, with the exciton 1s, 2s, and 3s states each represented by a Lorentzian peak resonance. The individual peak parameters are adjusted to match the measured reflectance contrast derivatives taking into account multi-layer interference effects in the studied structure using a transfer-matrix formalism. This approach allows for a quantitative analysis of the exciton peak parameters, such as transition energies and linewidths, as well as their contributions to the optical absorption of the monolayer. Additional details of the experimental procedure and data analysis are provided in the ESI.†

Results

The numerical evaluation of eqn (1) provides microscopic access to the excitonic absorption spectrum of an arbitrary TMD material. Fig. 2(a) shows the calculated spectra of an hBN-encapsulated WSe_2 monolayer at 5, 150 and 300 K, presented as function of energy relative to the exciton ground state resonance. At energies larger than the band gap we observe an absorption continuum reflecting the excitation of unbound electrons and holes. Furthermore, we obtain a hydrogen-like series of exciton resonances at their respective binding energies below the free particle bandgap. Apart from the strong absorption from the 1s ground state, we also observe higher excitonic resonances 2s, 3s,... with decreasing oscillator strength. We find about one order of magnitude difference between the oscillator strength of the 1s and the 2s state. With increasing temperatures, the absorption lines
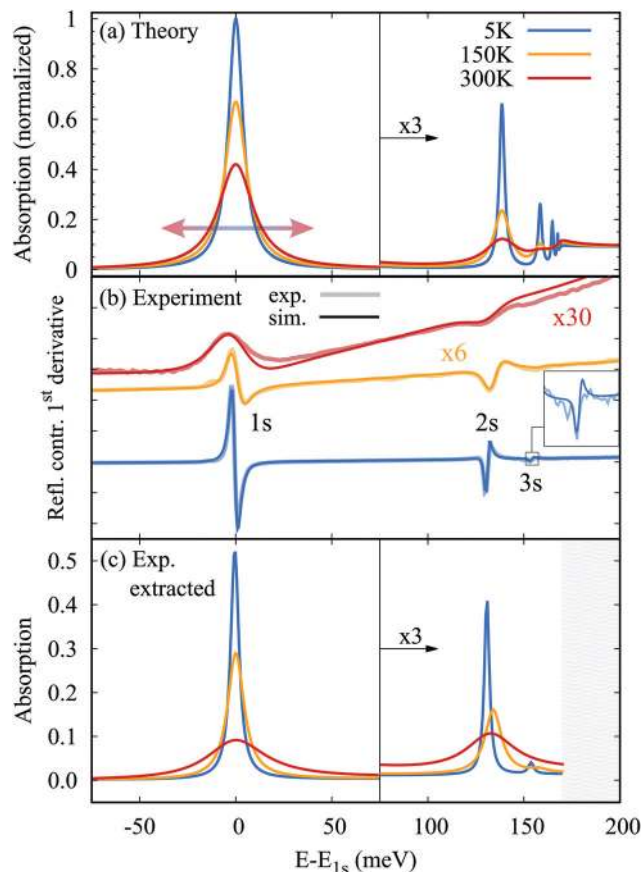
Fig. 2 (a) Theoretically calculated absorption spectra of an hBN-encapsulated WSe_2 monolayer at different temperatures. Due to the strong Coulomb interaction a clear hydrogen-like series of bound exciton resonances appears below the single particle bandgap. At low temperatures the intrinsic broadening allows to clearly resolve several excited states in the spectrum and the first excited state is visible even at 300 K. (b) Experimentally measured reflectance contrast derivatives of an hBN-encapsulated WSe_2 monolayer together with the simulated curves from the multi-Lorentzian model. The data are vertically offset and rescaled for clarity. (c) The corresponding extracted experimental absorption spectra for the contributions of the 1s, 2s, and 3s exciton resonances.

become broader due to an enhanced exciton–phonon interaction and the higher order resonances start to spectrally overlap. Nevertheless, over a range of temperatures the intrinsic broadening allows us to resolve several excited states in the spectrum. Importantly, the 2s resonance is clearly visible even at room temperature.

Experimentally measured data from hBN-encapsulated WSe_2 monolayer are presented in Fig. 2(b) as reflectance contrast derivatives together with the results of the multi-Lorentzian simulation and in (c) as the corresponding extracted experimental absorption spectra at 5, 150 and 300 K. The absorption is shown only for the contributions of the three exciton states appearing in the measured spectra and considered for the data analysis. The 1s and 2s exciton states are clearly observed at all temperatures, while the 3s state is detected only for temperatures below 150 K, *cf.* zoom-in in Fig. 2(b). As result of the larger signal-to-noise ratio, the experi-

mental uncertainty for the linewidth of the 3s is larger than for the first two states. As the temperature increases, the exciton peaks broaden under conservation of both peak areas and relative energy positions within a few meV. All changes are continuous, as further illustrated by the full temperature series presented in the ESI.†

In the following, we analyze the temperature dependence of the homogeneous total linewidth in the absorption, defined as full-width-at-half-maximum, and discuss the underlying microscopic scattering mechanisms. Fig. 3 shows the line-width as a function of the lattice temperature for the (a) 1s, (b) 2s and (c) 3s states. The black points show the linewidth extracted from reflectance contrast measurements with a dashed line included as guide to the eye. Theoretical results are presented as a color-coded decomposition illustrating the individual contributions from different scattering channels. Specifically, these include radiative broadening (yellow), phonon absorption (orange), phonon emission (red) and intervalley scattering processes (light and dark blue), as illustrated in Fig. 1.

The broadening of the 1s ground state is determined by the three channels depicted in Fig. 1: (i) a temperature indepen-dent broadening of about 2.5 meV results from the coherent radiative decay of the excitonic polarization (yellow area in Fig. 3(a)). (ii) Since 1s is the energetically lowest spin-like state at the K point, the only efficient intravalley phonon scattering process is the absorption of long range, small momentum acoustic phonons giving rise to a linear increase of the line-width with temperature (orange area). (iii) Finally, there is also scattering towards intervalley exciton states. These include, in particular the K–Λ excitons (corresponding to transition from K in the valence band to Λ in conduction band), which due to the two times higher electron mass at the Λ valley have a larger binding energy than the direct K–K exciton. In tungsten-based TMDs the electronic band splitting between K and Λ point turns out to be smaller than the difference in exciton binding energies, so that the dark K–Λ state is energetically below the bright state. In addition, the valley dependent spin–orbit splitting of the conduction band also gives rise to lower lying K–K′ excitons in tungsten-based TMDs. Therefore, inter-valley scattering *via* emission of phonons is very efficient in tungsten based TMDs and provides a significant contribution to the linewidth even at 0 K (light and dark blue area in Fig. 3(a)).[20] For the investigated, prototypical case of hBN-encapsulated WSe$_2$, we find an additional broadening of 3.9 meV at 0 K due to inter-valley relaxation.
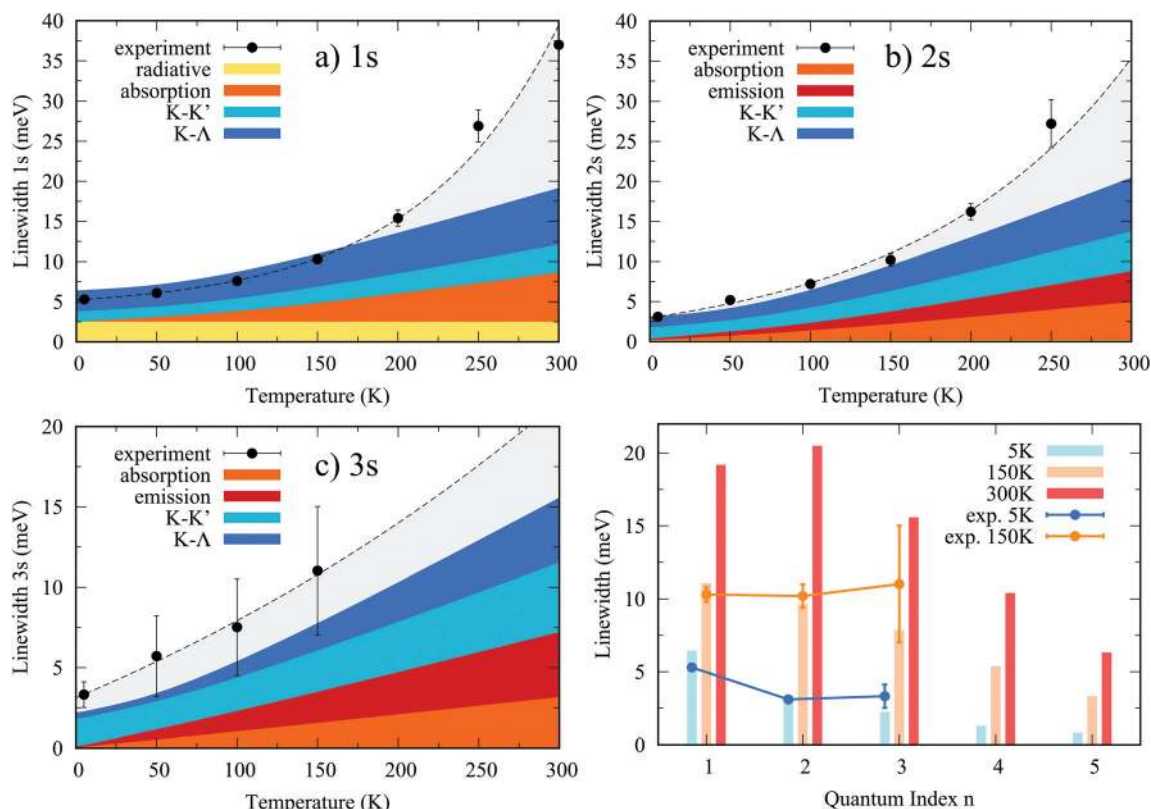
Fig. 3 Temperature-dependent linewidths of the (a) 1s, (b) 2s, and (c) 3s A exciton. The black points with error bars show the linewidth extracted from reflectance contrast measurements (dashed line shows a guide-to-the-eye using an exponential fit function). The theoretically calculated homogeneous linewidths are decomposed and color-coded in contributions of radiative decay, intravalley absorption/emission and intervalley scat-tering into the indirect K–Λ and K–K′ exciton, cf. Fig. 1. (d) The linewidth of the bright ns excitons as function of n for different temperatures. The microscopic model yields a decreasing trend for high n resulting from a reduced phonon scattering efficiency for excited states.

Interestingly when comparing the excited states with the ground state we find that, although the underlying scattering mechanisms include additional processes, the total broadening of 5 to 20 meV is comparable for all three states. In addition to the mentioned scattering channels, the 2s and 3s excitons can efficiently scatter to lower lying states within the same valley *via* emission of phonons (*cf.* red arrows in Fig. 1). Furthermore, there are more intervalley scattering channels available for excited states, since here transitions to *e.g.* K–Λ 2p states become possible. Therefore, these processes contribute to additional broadening of the exciton resonances with increasing quantum number n. However, we observe both in theory and experiment a similar broadening for 1s, 2s and 3s and even a decreased linewidth for the excited states at low temperatures.

To understand this somewhat counter-intuitive result we have to consider the influence of the exciton wavefunctions on radiative and non-radiative transition probabilities. With increasing principal quantum index n, exciton orbital functions become larger in space, which decreases the radiative recombination efficiency $\propto |\Phi_\nu(r = 0)|^2$, *cf.* eqn (2). This explains the strong reduction of the radiative broadening from about 2.5 meV for 1s to about 0.2 meV for 2s (yellow area in Fig. 3). Moreover, the spatially larger orbitals of excited states correspond to narrower wavefunctions in Fourier (momentum) space. Since the phonon-scattering efficiency is given by the overlap of initial and final state wavefunctions in momentum space, *cf.* eqn (4), larger exciton radii in real space lead to smaller scattering efficiencies per channel reflecting the reduced quantum mechanical momentum uncertainty.[35] Furthermore, the spatial oscillation of the wavefunctions of excited states additionally quenches the overlap integral in eqn (4). For the absorption of long range acoustic phonons *via* ns → ns (orange contributions in Fig. 3), the reduced scattering efficiency can be shown analytically by considering the excitonic form factor. Due to the small momentum transfer q_0 for these processes, it holds $\Gamma_{\nu \to \nu} \propto \langle \nu | e^{iq_0 r} | \nu \rangle \approx 1 - \frac{1}{2} q_0^2 \langle \nu | r^2 | \nu \rangle$. Since $\langle \nu | r^2 | \nu \rangle$ is a measure of the spatial variance of the probability function $|\Phi_\nu(r)|^2$, we find a decreased efficiency for the phonon absorption due to the increased orbital size of 2s and 3s excitons. As result, we find that in spite of the drastically increasing number of scattering channels for excited states, the scattering efficiency $G_{\lambda q}^{\nu \mu}$ for each of these channels can decrease even stronger. In these cases the linewidth decreases with the quantum index n.

The additional phonon emission channels into 2p states of K–K and K–Λ excitons compensate the loss of oscillator strength and scattering efficiency for the 2s state, *cf.* Fig. 3(b), yielding a comparable broadening at higher temperatures for both 1s and 2s states. However, the above discussed quenching of individual transition probabilities already gives rise to narrower 3s lines (Fig. 3(c)) despite an even larger phase space of lower lying final states and associated emission relaxation channels. In particular, scattering into the K′-valley becomes more dominant, since the 3s state lies energetically above the free particle continuum of the K–K′ exciton providing a large phase space of final quasi-resonant states.

Finally, in Fig. 3(d) we show the homogeneous linewidth of exciton resonances ns as a function of their principal quantum number n for three different temperatures. As discussed above, the increased phase space leads to a slight increase of the linewidth from 1s to 2s at room temperature. However, for larger quantum numbers or at lower temperatures we observe a clear monotonous decrease of the broadening with n, reflecting the strongly decreasing scattering cross section due to the larger exciton Bohr radii. We predict significantly narrower linewidths of 4s and 5s states compared to the 1s ground state. Our prediction is qualitatively similar to the findings of the experimental and theoretical studies on Rydberg excitons in copper oxide,[36,37] where a decrease of the linewidth with the principal quantum number n was found.

For the three lowest exciton states, we obtain a good agreement between experimentally observed and theoretically predicted linewidths with reasonable quantitative deviations, which are discussed in the following. First, the theoretical model overstimates the linewidth of the 1s state by about 1 meV at low temperatures. In line with previous studies on TMD/hBN hetreostructures,[11,12] we find that the line broadening becomes strongly reduced in encapsulated samples. As for example shown in four-wave mixing experiments performed by Jakubczyk *et al.*,[38] we assume that the linewidth in these systems approaches the intrinsic limit. Therefore the error bars for the experimentally measured linewidths correspond to confidence intervals of the fit procedure, which are very small for the 5 K measurements. Moreover, we want to emphasize that the theoretical model is entirely based on parameters from *ab initio* calculations in literature without any adjustments. Since these parameters correspond to free standing monolayers, the slight overestimation of the linewidth in our model might result from substrate effects, *e.g.* small strain values induced by the hBN encapsulation. Moreover, the applied Born-Markov approximation and the deformation potential approach give rise to further theoretical uncertainties. Note, that the aim of our work is not a perfect quantitative agreement with the experiment, but rather a fundamental understanding of the observed trend for the excited exciton states.

Secondly, to reproduce the strong increase in the linewidth up to room temperature (grey-shaded area), one needs to take into account the appearance of phonon sidebands.[19,42] These effects in addition to the homogenous contributions (coherence lifetime) presented here give rise to a super-linear increase of the full peak linewidth at elevated temperatures. The emergence of asymmetric phonon side bands is already indicated in the deviation of the measured reflectance spectra from the simulated symmetric Lorentzians around the 1s state at 300 K, *cf.* Fig. 2(b). As reported in ref. 19 phonon-assisted optical transitions significantly influence the exciton lineshape in WSe₂ for temperatures above 150 K, since here the energetically lower lying dark states give rise to side bands below and above the exciton main resonance. In ref. 19 a ratio between FWHM and homogeneous linewidth of about 0.58 has been reported, which corresponds well to the ratio between the calculated 19 meV homogeneous linewidth and the measured 37 meV FWHM.

Finally, in this study we have focused on the intrinsic broadening mechanisms in a homogeneous system, *i.e.* assuming a perfect lattice periodicity and a spatially constant dielectric background. This assumption has turned out to widely reproduce the linewidth in exfoliated, hBN-encapsulated TMDs, supporting the findings from recent four-wave mixing experiments.[38] However, effects resulting from inhomogeneities will have a much larger impact in non-encapsulated samples, *e.g.* as-exfoliated flakes on SiO_2 substrates. Here both, the spatial fluctuation of resonance energies due to dielectric inhomogeneities as well as the possible elastic scattering of excitons at lattice defects should contribute to the broadening of excited and ground state. The scattering with defects, in particular, is expected to stronger influence the lifetime of excited states in contrast to the ground state due to a smaller number of resonant final states for the latter, necessary for elastic scattering. Similarly, spatial variations of the band gap due to dielectric disorder should also affect the resonance energy of the excited states by a larger degree due to reduced cancellation effects of the bandgap renormalization and binding energy,[39] yielding an increasing inhomogeneous broadening with the quantum number n. Therefore, the small constant offset between the calculated intrinsic linewidth and the measured broadening of the 3s state of a few meV (Fig. 3(c)) can be assigned to the presence of residual inhomogeneities potentially remaining in the hBN-encapsulated samples.

Conclusion

We have presented a joint experiment-theory study addressing the microscopic mechanisms governing the intrinsic broadening of higher exciton states in atomically thin WSe_2 monolayers. We reveal both in experiment and theory that the higher excitonic states surprisingly show either a similar or even smaller linewidth compared to the exciton ground state – despite the larger number of final states for scattering events. Importantly, while the small Bohr radius of the ground state enables both strong light–matter coupling and efficient absorption of acoustic phonons, these processes become much weaker for excited states. The spatially extended orbital functions of excited states give rise to lower oscillator strength and reduced exciton–phonon scattering efficiency, resulting from smaller overlaps of initial and final state wavefunctions in momentum space. On the other hand, transitions into energetically lower lying p exciton states lead to an additional broadening mechanism resulting in comparable linewidths for the ground and excited exciton states. The gained insights should strongly contribute to the fundamental understanding of the exciton physics and carrier-lattice interactions in atomically thin transition metal dichalcogenide and guide future studies.

Conflicts of interest

There are no conflicts of interest to declare.

Acknowledgements

References

1 M. M. Ugeda, A. J. Bradley, S.-F. Shi, H. Felipe, Y. Zhang, D. Y. Qiu, W. Ruan, S.-K. Mo, Z. Hussain, Z.-X. Shen, *et al.*, *Nat. Mater.*, 2014, **13**, 1091.

2 G. Berghäuser and E. Malic, *Phys. Rev. B: Condens. Matter Mater. Phys.*, 2014, **89**, 125309.

3 A. Steinhoff, J.-H. Kim, F. Jahnke, M. Roĺsner, D.-S. Kim, C. Lee, G. H. Han, M. S. Jeong, T. Wehling and C. Gies, *Nano Lett.*, 2015, **15**, 6841–6847.

4 G. Wang, A. Chernikov, M. M. Glazov, T. F. Heinz, X. Marie, T. Amand and B. Urbaszek, *Rev. Mod. Phys.*, 2018, **90**, 021001.

5 T. Mueller and E. Malic, *npj 2D Mater. Appl.*, 2018, **2**, 29.

6 M. Baranowski, A. Surrente, L. Klopotowski, J. Urban, N. Zhang, D. K. Maude, K. Wiwatowski, S. Mackowski, Y.-C. Kung, D. Dumcenco, *et al.*, *Nano Lett.*, 2017, **17**, 6360–6365.

7 T. Deilmann and K. S. Thygesen, *Nano Lett.*, 2018, **18**, 1460–1465.

8 K. He, N. Kumar, L. Zhao, Z. Wang, K. F. Mak, H. Zhao and J. Shan, *Phys. Rev. Lett.*, 2014, **113**, 026803.

9 A. Chernikov, T. C. Berkelbach, H. M. Hill, A. Rigosi, Y. Li, O. B. Aslan, D. R. Reichman, M. S. Hybertsen and T. F. Heinz, *Phys. Rev. Lett.*, 2014, **113**, 076802.

10 H. M. Hill, A. F. Rigosi, C. Roquelet, A. Chernikov, T. C. Berkelbach, D. R. Reichman, M. S. Hybertsen, L. E. Brus and T. F. Heinz, *Nano Lett.*, 2015, **15**, 2992–2997.

11 A. V. Stier, N. P. Wilson, K. A. Velizhanin, J. Kono, X. Xu and S. A. Crooker, *Phys. Rev. Lett.*, 2018, **120**, 057405.

12 C. Robert, M. Semina, F. Cadiz, M. Manca, E. Courtade, T. Taniguchi, K. Watanabe, H. Cai,

S. Tongay, B. Lassagne, *et al.*, *Phys. Rev. Mater.*, 2018, **2**, 011001.

13 A. Steinhoff, M. Rosner, F. Jahnke, T. Wehling and C. Gies, *Nano Lett.*, 2014, **14**, 3743–3748.

14 A. Raja, A. Chaves, J. Yu, G. Arefe, H. M. Hill, A. F. Rigosi, T. C. Berkelbach, P. Nagler, C. Schüller, T. Korn, *et al.*, *Nat. Commun.*, 2017, **8**, 15251.

15 P. Steinleitner, P. Merkl, A. Graf, P. Nagler, K. Watanabe, T. Taniguchi, J. Zipfel, C. SchuÍLller, T. Korn, A. Chernikov, *et al.*, *Nano Lett.*, 2018, **18**, 1402–1409.

16 A. Singh, A. Knorr, C. K. Dass, C.-H. Chen, E. Malic, G. Moody, G. Clark, G. Berghäuser, K. Hao, K. Tran, *et al.*, *Nat. Commun.*, 2015, **6**, 8315.

17 M. Palummo, M. Bernardi and J. C. Grossman, *Nano Lett.*, 2015, **15**, 2794–2800.

18 P. Dey, J. Paul, Z. Wang, C. Stevens, C. Liu, A. Romero, J. Shan, D. Hilton and D. Karaiskaj, *Phys. Rev. Lett.*, 2016, **116**, 127402.

19 D. Christiansen, M. Selig, G. Berghäuser, R. Schmidt, I. Niehues, R. Schneider, A. Arora, S. M. de Vasconcellos, R. Bratschitsch, E. Malic, *et al.*, *Phys. Rev. Lett.*, 2017, **119**, 187402.

20 M. Selig, G. Berghäuser, A. Raja, P. Nagler, C. Schüller, T. F. Heinz, T. Korn, A. Chernikov, E. Malic and A. Knorr, *Nat. Commun.*, 2016, **7**, 13279.

21 I. Niehues, R. Schmidt, M. DruÍLppel, P. Marauhn, D. Christiansen, M. Selig, G. BerghaÍLuser, D. Wigger, R. Schneider, L. Braasch, *et al.*, *Nano Lett.*, 2018, **18**, 1751–1757.

22 S. Koch, M. Kira, G. Khitrova and H. Gibbs, *Nat. Mater.*, 2006, **5**, 523–531.

23 M. Kira and S. Koch, *Prog. Quantum Electron.*, 2006, **30**, 155–296.

24 H. Haug and S. W. Koch, *Quantum Theory of the Optical and Electronic Properties of Semiconductors*, World Scientific Publishing Company, 5th edn, 2009.

25 D. Xiao, G.-B. Liu, W. Feng, X. Xu and W. Yao, *Phys. Rev. Lett.*, 2012, **108**, 196802.

26 M. Selig, G. Berghäuser, M. Richter, R. Bratschitsch, A. Knorr and E. Malic, *2D Mater.*, 2018, **5**, 035017.

27 N. Rytova, *Proc. MSU, Phys., Astron.*, 1967, **3**, 30.

28 L. Keldysh, *JETP Lett.*, 1979, **29**, 658.

29 A. Kormányos, G. Burkard, M. Gmitra, J. Fabian, V. Zólyomi, N. D. Drummond and V. FalâĂŹko, *2D Mater.*, 2015, **2**, 022001.

30 A. Laturia, M. L. Van de Put and W. G. Vandenberghe, *npj 2D Mater. Appl.*, 2018, **2**, 6.

31 A. Knorr, S. Hughes, T. Stroucken and S. Koch, *Chem. Phys.*, 1996, **210**, 27–47.

32 A. Thränhardt, S. Kuckenburg, A. Knorr, T. Meier and S. Koch, *Phys. Rev. B: Condens. Matter Mater. Phys.*, 2000, **62**, 2706.

33 S. Brem, M. Selig, G. Berghaeuser and E. Malic, *Sci. Rep.*, 2018, **8**, 8238.

34 Z. Jin, X. Li, J. T. Mullen and K. W. Kim, *Phys. Rev. B: Condens. Matter Mater. Phys.*, 2014, **90**, 045422.

35 Y. Toyozawa, *Prog. Theor. Phys.*, 1958, **20**, 53–81.

36 T. Kazimierczuk, D. Fröhlich, S. Scheel, H. Stolz and M. Bayer, *Nature*, 2014, **514**, 343.

37 H. Stolz, F. Schöne and D. Semkat, *New J. Phys.*, 2018, **20**, 023019.

38 T. Jakubczyk, G. Nayak, L. Scarpelli, W.-L. Liu, S. Dubey, N. Bendiab, L. Marty, T. Taniguchi, K. Watanabe, F. Masia, *et al.*, *ACS Nano*, 2019, **13**(3), 3500–3511.

39 Y. Cho and T. C. Berkelbach, *Phys. Rev. B*, 2018, **97**, 041409.

40 P. Merkl, F. Mooshammer, P. Steinleitner, A. Girnghuber, K.-Q. Lin, P. Nagler, J. Holler, C. Schüller, J. M. Lupton, T. Korn, S. Ovesen, S. Brem, E. Malic and R. Huber, *Nat. Mater.*, 2019, **18**, 691–696.

41 O. B. Aslan, M. Deng and T. F. Heinz, *Phys. Rev. B*, 2018, **98**, 115308.

42 S. Brem, A. Ekman, D. Christiansen, F. Katsch, M. Selig, C. Robert, X. Marie, B. Urbaszek, A. Knorr and E. Malic, 2019, arXiv:1904.04711.